PERGAMON

International Journal of Solids and Structures 37 (2000) 4715–4732

INTERNATIONAL JOURNAL OF SOLIDS and STRUCTURES

www.elsevier.com/locate/ijsolstr

A three-dimensional nonlinear viscoelastic constitutive model of solid propellant

Gyoo-Dong Jung[a], Sung-Kie Youn[b,*], Bong-Kyu Kim[b]

[a]*Fourth R&D Center, Agency for Defense Development, Yusung, P.O. Box 35-4, Taejon 305-600, South Korea*
[b]*Department of Mechanical Engineering, Korea Advanced Institute of Science and Technology, 373-1, Kusung, Yusung, Taejon 305-701, South Korea*

Received 23 August 1998

Abstract

A nonlinear viscoelastic constitutive model for the solid propellant is proposed. In their earlier work, the authors have developed an isotropic constitutive model and verified it for one-dimensional case. In the present work, the validity of the model is extended to three-dimensional cases. Also, implementation of the model into a commercial code for the use of the constitutive model in the finite element analysis of solid propellant is discussed. Large deformation, dewetting and cyclic loading effects are treated as main sources of nonlinear behavior of the solid propellant. The softening of the solid propellant due to dewetting is treated by the modulus decrease. The nonlinearities during cyclic loading are accounted for by the functions of the octahedral shear strain measure. The constitutive equation is implemented into a finite element code for the analysis of propellant grains. A commercial finite element package 'ABAQUS' is used for the analysis and the model is introduced into the code through a user subroutine. The model is evaluated with different loading conditions and the predicted values are in good agreement with the biaxial test results.

Keywords: Viscoelasticity; Constitutive equation; Solid propellant; Dewetting; Cyclic loading

1. Introduction

Composite solid propellants are considered as lightly cross-linked, long chain polymers filled with solid particles. These materials exhibit highly nonlinear viscoelastic response due to the damage process such as the Mullin's effect, dewetting, nonlinear time–temperature effect and large deformation (Farris and Schapery, 1973). These microscopic changes cause the solid propellant to lose its initial stiffness and

* Corresponding author. Fax: +82-42-861-1694.
E-mail address: skyoun@sorak.kaist.ac.kr (S.K. Youn).

0020-7683/00/$ - see front matter
PII: S0020-7683(99)00180-8

change its bulk behavior from incompressible to compressible behavior. The very complicated nonlinear behavior of solid propellants also comes from the features associated with time–temperature effects(Ravichandran and Liu, 1995). Recently, Jung and Youn (1999) proposed a constitutive model, which includes the effect of the large deformation, stress softening by dewetting in micro structure and nonlinearities in the cyclic loading on the overall stress–strain behavior. This model was experimentally verified on the various uniaxial loading conditions. In the present study, the model is extended to a general three dimensional state for the stress analysis of propellant grains. In extending the existing model, the cyclic loading damage functions are modified to improve stress prediction accuracy. A commercial finite element package 'ABAQUS' is adopted for analysis and the developed constitutive equation is implemented through a user subroutine, UMAT. The validity is tested using the strip biaxial specimens with circular holes subjected to different loading conditions.

2. The constitutive model

2.1. The developed constitutive model

In the constitutive model developed by Jung and Youn (1999), it is assumed that the time characteristics of the free energy of solid propellant do not change by damage and the propellant is homogeneous and isotropic. In this case, the free energy function of the propellant can be regarded as the free energy of the undamaged propellant multiplied by a damage function. Damages considered are the dewetting phenomena and the nonlinearities inherent in the load–unload cycles. A viscoelastic dewetting criterion is derived from the law of energy conservation. The damage due to filler dewetting causes decrease in effective moduli of the propellant. The reduction in effective moduli is regarded as the results of the decrease in the effective filler volume fraction. The function of generalized octahedral shear stain is introduced as the medium of cyclic load effect. The large strain capability of solid propellant requires that the stress–strain relation be formulated in terms of the appropriate stress and strain tensors. For this, Simo's model (Simo, 1987) for stress–strain behavior is adopted and modified. Simo's constitutive relation is modified by generalizing the elastic bulk response to viscoelastic one and introducing the volumetric and deviatoric damage functions, D_v, D_d. The model was verified in the uniaxial stress field. While some models require many phenomenological nonlinear functions (Özüpek and Becker, 1996; Park and Schapery, 1997), this model has the advantages, in that, it reflects the realistic viscoelastic dewetting behavior as well as the effects of the properties of the individual constituent in the solid propellant. The resulting constitutive equation is of the following form.

$$S(t) = D_v J C^{-1} P I + D_d J^{-2/3} \mathrm{DEV}[H] \tag{1}$$

where

$$P = \int_0^t \frac{K(\eta - \eta')}{K_0} \frac{\partial}{\partial \xi} \left(\frac{\partial U^0}{\partial J} \right) \mathrm{d}\xi \tag{2}$$

$$H = \int_0^t \frac{G(\eta - \eta')}{G_0} \frac{\partial}{\partial \xi} \mathrm{DEV} \left(\frac{\partial \bar{\Psi}^0}{\partial \bar{E}} \right) \mathrm{d}\xi \tag{3}$$

$S(t)$ is the second Piola–Kirchhoff stress, J the determinant of the deformation gradient, $\bar{E}$ the volume preserving part of Green strain E, $K(t) = K_\infty + \sum_{i=1}^{n} K_i \, \mathrm{e}^{-t/\tau_i}$ the bulk relaxation modulus, $G(t) = G_\infty +$

$\sum_{i=1}^{n} G_i \, e^{-t/\tau_i}$ the shear relaxation modulus, $K_0 = K_\infty + \sum_{i=1}^{n} K_i$, $G_0 = G_\infty + \sum_{i=1}^{n} G_i$, $\mathrm{DEV}[\bullet] = (\bullet) - \frac{1}{3}[C : (\bullet)]C^{-1}$ and C the Cauchy–Green tensor. Also, $U^0(J)$ and $\bar{\Psi}^0(\bar{E})$ are the uncoupled volumetric and deviatoric parts of the initial elastic stored energy, D_v and D_d the volumetric and deviatoric damage functions, respectively. Also

$$\eta(t) = \int_0^t \frac{d\tau}{a_T[T(\tau)]}, \qquad \eta(\xi) = \int_0^\xi \frac{d\tau}{a_T[T(\tau)]} \tag{4}$$

are the reduced times and a_T the time–temperature shift factor.

In this model, the volumetric and deviatoric damages caused by dewetting are defined as follows:

$$\hat{D}_v = \frac{K_D}{K} \tag{5}$$

$$\hat{D}_d = \frac{G_D}{G} \tag{6}$$

where K_D and G_D are the decreased propellant moduli due to dewetting. To calculate K_D and G_D, we need to know when debonding will occur and how much reduction of the moduli caused by dewetting. Therefore dewetting criterion and the method that calculates modulus decrease due to debonding is essential. From the energy balence consideration for dewetting following viscoelastic dewetting criterion has been derived (Jung and Youn, 1999).

$$\frac{1}{4G_0^2}\frac{dG_0}{dc} S'_{ij} S'_{ij} + \frac{1}{18K_0^2}\frac{dK_0}{dc}\sigma_{kk}\sigma_{ii} = \frac{6}{R} G_c \tag{7}$$

where c is the current filler volume fraction, S'_{ij} and σ_{ii} the deviatoric and volumetric stresses, R the filler radius, G_c the adhesion energy between the filler and binder of solid propellant. From Eq. (7) we could say that large filler particles debond first under the same stress level and to be able to determine the reduction in particle volume fraction due to dewetting under the current stress level, we need filler size distribution like Fig. 7. The statistical distribution of filler particle size has been obtained by using particle sizer. In the implementation, the filler particles are divided into large number of groups with different radii. The debonded particles are eliminated from the propellants and replaced with voids of equal sizes. The dewetting causes loss of reinforcement in the propellant. Modulus changes based on filler volume fraction are calculated using the Farber–Farris equations (Farber and Farris, 1987):

$$\frac{dG}{dc} = \frac{-15G(1+\nu)\left(1 - \dfrac{G_i}{G}\right)}{\left\{7 - 5\nu + 2(4-5\nu)\dfrac{G_i}{G}\right\}[1-c]}$$

$$\frac{dK}{dc} = \frac{K_i - K}{\left\{1 + \dfrac{K_i - K}{K + 4/3G}\right\}(1-c)} \tag{8}$$

where G is the shear modulus of propellant, ν the Poisson's ratio of propellant, K the bulk modulus of propellant, and K_i, G_i are the moduli of filler. The damage caused by dewetting can be evaluated by following procedure. Firstl, the stress is calculated for given deformation history. Secondly, dewetting occurrence is determined by Eq. (7) for current group of undewetted filler particles with largest radius.

And then if dewetting occurs, the particles in the current group are removed to yield new filler volume fraction. Then K_D and G_D are calculated using Eq. (8). Finally, damages due to dewetting are calculated by Eqs. (5) and (6). Above procedure is repeated until no dewetting occurs.

The cyclic load effects are characterized as the rapid decrease in stress during unloading and large amount of hysteresis in load–unload cycles. The cyclic load effects depend on current shear strain and maximun shear strain during the loading history, which is known through experiment (Swanson and Christensen, 1983). Thus, the nonlinearities during cyclic loading are accounted for by the following function f which depends on the generalized octahedral shear strain measure (Özüpek and Becker, 1996).

$$f = \begin{cases} f_u\left(\dfrac{\bar{I}_\gamma}{\bar{I}_{\gamma_{max}}}\right) & \text{at unloading from loading} \\ f_u\left(\dfrac{\bar{I}_\gamma}{\bar{I}_{\gamma_{max}}}\right)\cdot f_{r/u}(\bar{I}_{rel}) & \text{at reloading or unloading from reloading} \\ 1 & \text{at loading} \end{cases} . \tag{9}$$

where $\bar{I}_\gamma = \frac{1}{6}(2\bar{I}_1^2 - 6\bar{I}_2)^{1/2}$, $\bar{I}_1$ and $\bar{I}_2$ are the first and second invariant of $\bar{C} = J^{-2/3}C$, $f_{r/u} = f_r/f_u$, $\bar{I}_{rel} = \frac{\bar{I}_\gamma - \bar{I}_{\gamma_{min}}}{\bar{I}_{\gamma_{max}} - \bar{I}_{\gamma_{min}}}$, $\bar{I}_{\gamma_{min}}$ is the value at the end of unloading. f_u and f_r are obtained from the comparison between calculated stresses without f and measured ones in unloading and reloading test. Thus, total volumetric and deviatoric damages used in this model are defined as follows:

$$D_v = \hat{D}_v f\left(\frac{\bar{I}_\gamma}{\bar{I}_{\gamma_{max}}}\right) \tag{10}$$

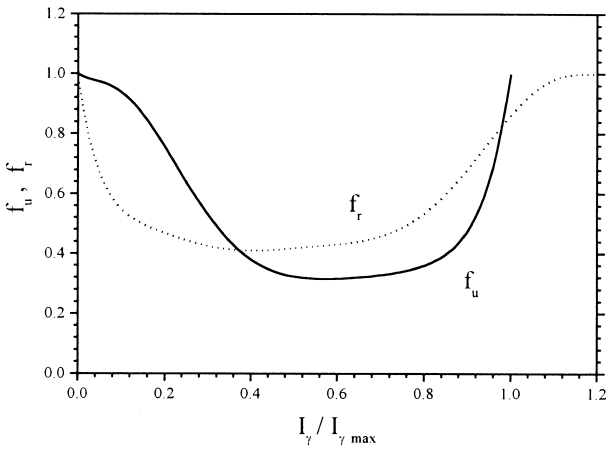

Fig. 1. Unloading and reloading functions, f_u, f_r.

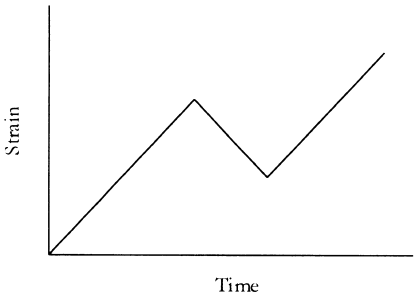

Fig. 2. Imposed strain history for partial unloading and reloading.

$$D_{\mathrm{d}} = \hat{D}_{\mathrm{d}} f\left(\frac{\bar{I}_{\gamma}}{\bar{I}_{\gamma_{\max}}}\right) \tag{11}$$

2.2. Improved cyclic loading damage function

The unloading and reloading functions, f_{u} and f_{r} are shown in Fig. 1. These functions are obtained from the uniaxial cyclic test with constant strain amplitude (0–20% strain) at 50%/min, 20°C. This process is well explained by Jung and Youn (1999). For the reloading after partial unloading condition as in Fig. 2, the function f evaluated by Eq. (9) is shown as the triangular symbols in Fig. 3. In Fig. 3, the values of f turn out to be impractically small or large when the load direction is reversed. This does

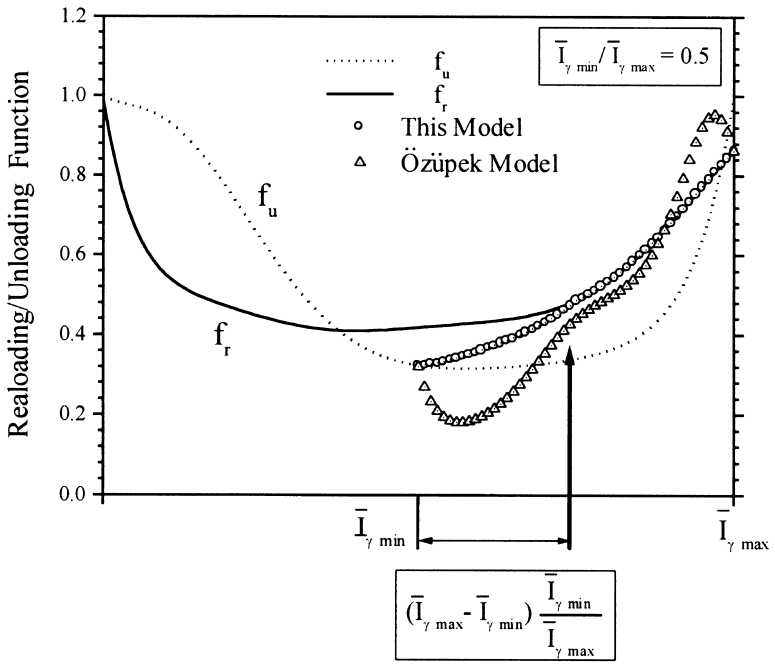

Fig. 3. Behavior of function f at reloading from unloading.

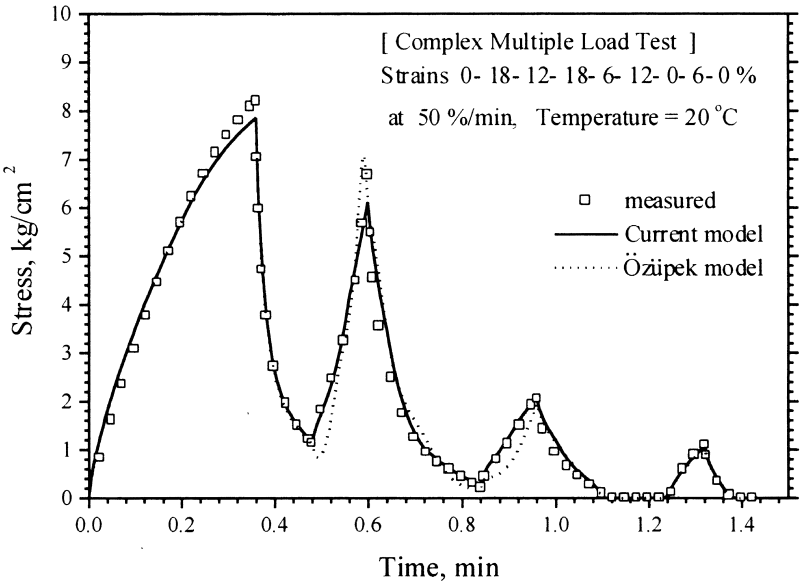

Fig. 4. Uniaxial complex multiple load test at 20°C.

not reflect the real behavior of propellant and make the convergence rate slow when used in the finite element analysis. Therefore, the form of f in Eq. (9) is modified for the reloading or unloading from reloading conditions as follows:

$$f\left(\frac{\bar{I}_\gamma}{\bar{I}_{\gamma_{\max}}}\right) = \begin{cases} f_u & \text{at unloading from loading} \\ (1-\tilde{I}_{rel})f_u + \tilde{I}_{rel}f_r & \text{at reloading or unloading from reloading} \\ 1 & \text{at loading} \end{cases}. \tag{12}$$

where

$$\tilde{I}_{rel} = \begin{cases} \bar{I}_{rel} + \dfrac{\bar{I}_\gamma}{\bar{I}_{\gamma_{\min}}} - 1 & \text{if } \bar{I}_{\gamma_{\min}} \le \bar{I}_\gamma < \bar{I}_{\gamma_{\min}} + \left(\bar{I}_{\gamma_{\max}} - \bar{I}_{\gamma_{\min}}\right)\dfrac{\bar{I}_{\gamma_{\min}}}{\bar{I}_{\gamma_{\max}}} \\ 1 & \text{if } \bar{I}_\gamma \ge \bar{I}_{\gamma_{\min}} + \left(\bar{I}_{\gamma_{\max}} - \bar{I}_{\gamma_{\min}}\right)\dfrac{\bar{I}_{\gamma_{\min}}}{\bar{I}_{\gamma_{\max}}} \end{cases}. \tag{13}$$

In Eq. (12), the values of f are considered to vary linearly from f_u to f_r during $\bar{I}_{\gamma_{\min}} < \bar{I}_\gamma < \bar{I}_{\gamma_{\min}} + (\bar{I}_{\gamma_{\max}} - \bar{I}_{\gamma_{\min}})\frac{\bar{I}_{\gamma_{\min}}}{\bar{I}_{\gamma_{\max}}}$. This results in smooth transition of f between f_u and f_r when the load direction is reversed. This is shown as the circular legend in Fig. 3. When this improved form of f is applied for the uniaxial complex multiple load test conducted by Jung and Youn (1999), the comparisons of the predicted and observed stress–strain behaviors are shown in Fig. 4. The modified form of f, Eq. (12), shows more accurate stress predictions than the previous one, Eq. (9), at cyclic loading condition.

3. Implementation of constitutive equation

For the analysis of three-dimensional finite element analysis, the constitutive equation is implemented

in the user subroutine UMAT of ABAQUS code. This can be done by updating the stresses at the end of the increment and providing the tangent stiffness using the presented constitutive model (ABAQUS User's Manual, 1996).

3.1. Stress representation

For finite strain applications, the interface for subroutine UMAT requires Cauchy stress components as stress measures. The second Piola–Kirchhoff stress in the constitutive equation, Eq. (1), is converted to Cauchy stress by the relation $\sigma = \frac{1}{J}FSF^{\mathrm{T}}$. The constitutive equation in terms of Cauchy stress becomes as follows:

$$\sigma = D_{\mathrm{v}}PI + D_{\mathrm{d}}\frac{1}{J}\mathrm{dev}\left[\bar{F}H\bar{F}^{\mathrm{T}}\right] \tag{14}$$

where $\mathrm{dev}[\bullet] = \bullet - \frac{1}{3}(\bullet{:}I)I$ and $\bar{F} = J^{-1/3}F$ is volume preserving deformation gradient. The calculation of the convolution integrals, H and P, is accomplished by using a numerical algorithm developed by Taylor et al. (1970). By using the Prony series representations of the relaxation moduli and approximating the integrals of each series terms, H and P are arranged in the following forms.

$$P_{n+1} = \bar{K}_{\infty}\bar{P}_{n+1} + \sum_{i=1}^{n}\bar{K}_i\bar{P}^i_{n+1} \tag{15}$$

$$H_{n+1} = \bar{G}_{\infty}\Pi_{n+1} + \sum_{i=1}^{n}\bar{G}_i\bar{H}^i_{n+1} \tag{16}$$

where $\bar{K}_{\infty} = \frac{K_{\infty}}{K_0}$, $\bar{K}_i = \frac{K_i}{K_0}$, $\bar{G}_{\infty} = \frac{G_{\infty}}{G_0}$, $\bar{G}_i = \frac{G_i}{G_0}$ are modulus ratios, $\bar{P} = \frac{\partial U^0}{\partial J}$, $\Pi = \mathrm{DEV}(\frac{\partial \bar{\Psi}^0}{\partial \bar{E}})$, $\bar{P}^i_{n+1} = \mathrm{e}^{-\Delta\eta/\tau_i}\bar{P}^i_n + \frac{\tau_i(1-\mathrm{e}^{-\Delta\eta/\tau_i})}{\Delta\eta}(\bar{P}_{n+1} - \bar{P}_n)$, $\bar{H}^i_{n+1} = \mathrm{e}^{-\Delta\eta/\tau_i}\bar{H}^i_n + \frac{\tau_i(1-\mathrm{e}^{-\Delta\eta/\tau_i})}{\Delta\eta}(\Pi_{n+1} - \Pi_n)$ and the right subscripts mean time steps, that is, $\bar{P}_{n+1}$ means the value of $\bar{P}$ at time t_{n+1}.

3.2. Tangent stiffness representation

In ABAQUS (ABAQUS Theory Manual, 1996), Kirchhoff stress increment $\mathrm{d}_t\tau$ is represented by spin tensor W and tangent stiffness $\mathscr{L}^J$ as

$$\mathrm{d}_t\tau = \mathrm{d}W_t\tau + {}_t\tau\mathrm{d}W^{\mathrm{T}} + \mathscr{L}^J\mathrm{d}\varepsilon \tag{17}$$

By letting $\partial S/\partial E$ as $\mathscr{L}$, using the relation between 2nd Piola–Kirchhoff stress S and Cauchy stress σ and introducing time derivative of Kirchhoff stress, τ, $\mathscr{L}^J$ is represented by the following relation

$$\mathscr{L}^J_{ijkl} = \mathscr{C}_{ijkl} + \delta_{ik}\sigma_{jl} + \sigma_{ik}\delta_{jl} \tag{18}$$

where

$$\mathscr{C}_{ijkl} = \frac{1}{J}F_{ip}F_{jq}F_{kr}F_{ls}\mathscr{L}_{pqrs} \tag{19}$$

$\mathscr{L}$ is obtained by differentiating Eq. (1) by Green strain E as

$$\mathscr{L} = D_{\mathrm{v}}\left[\left(\alpha J^{2}\frac{\partial^{2}U^{0}}{\partial J^{2}} + JP\right)C^{-1}\otimes C^{-1} - 2PI_{C^{-1}}\right] + D_{\mathrm{d}}\mathscr{L}_{\mathrm{dev}} + \frac{S}{f}\otimes\frac{\partial f}{\partial E} \tag{20}$$

where $\mathscr{L}_{\mathrm{dev}}$ is

$$J^{2/3}\mathscr{L}_{\mathrm{dev}} = -\frac{2}{3}\left(H\otimes C^{-1} + C^{-1}\otimes H\right) + \frac{2}{3}\left[\bar{G}_{\infty}\Pi{:}C + \sum_{i=1}^{n}\bar{G}_{i}\bar{H}_{i}{:}C\right]\left(I_{C^{-1}} + \frac{1}{3}C^{-1}\otimes C^{-1}\right)$$
$$+ \frac{2}{3}\beta\left(\frac{\partial\bar{\Psi}^{0}}{\partial\bar{E}}\right)\left(I_{C^{-1}} - \frac{1}{3}C^{-1}\otimes C^{-1}\right) + \beta J^{-2/3}\mathrm{DEV}\left[\frac{\partial^{2}\bar{\Psi}^{0}}{\partial\bar{E}^{2}}\right] \tag{21}$$

and

$$\mathrm{DEV}\left[\frac{\partial^{2}\bar{\Psi}^{0}}{\partial\bar{E}^{2}}\right] = \frac{\partial^{2}\bar{\Psi}^{0}}{\partial\bar{E}^{2}} - \frac{1}{3}\left(\frac{\partial^{2}\bar{\Psi}^{0}}{\partial\bar{E}^{2}}{:}C\right)\otimes C^{-1} - \frac{1}{3}C^{-1}\otimes\left(\frac{\partial^{2}\bar{\Psi}^{0}}{\partial\bar{E}^{2}}{:}C\right) + \frac{1}{9}\left(C{:}\frac{\partial^{2}\bar{\Psi}^{0}}{\partial\bar{E}^{2}}{:}C\right)C^{-1}\otimes C^{-1} \tag{22}$$

$$\alpha = \bar{K}_{\infty} + \sum_{i=1}^{n}\left[\bar{K}_{i}\frac{\tau_{i}(1-\mathrm{e}^{-\Delta\eta/\tau_{i}})}{\Delta\eta}\right] \tag{23}$$

$$\beta = \bar{G}_{\infty} + \sum_{i=1}^{n}\left[\bar{G}_{i}\frac{\tau_{i}(1-\mathrm{e}^{-\Delta\eta/\tau_{i}})}{\Delta\eta}\right] \tag{24}$$

$$(I_{C^{-1}})_{ijkl} = C^{-1}_{ik}C^{-1}_{jl} \tag{25}$$

Therefore, substituting Eq. (20) for Eq. (19) and simplifying gives

$$\mathscr{C} = D_{\mathrm{v}}\left[\left(\alpha J\frac{\partial^{2}U^{0}}{\partial J^{2}} + P\right)I\otimes I - 2P\tilde{I}\right] + D_{\mathrm{d}}\mathscr{C}_{\mathrm{dev}} + \mathscr{C}_{f} \tag{26}$$

where $\tilde{I}$ is the identity tensor of order 4. $\mathscr{C}_{\mathrm{dev}}$ and $\mathscr{C}_{f}$ are represented as:

$$\mathscr{C}_{f} = \frac{\sigma}{f}\otimes\frac{\partial f}{\partial\bar{I}_{\gamma}}\left[\frac{1}{12}\left(2\bar{I}_{1}^{2} - 6\bar{I}_{2}\right)^{-1/2}\left[-4\bar{I}_{1}\bar{B} + 12\bar{B}\bar{B}\right] - \frac{1}{9}\left(2\bar{I}_{1}^{2} - 6\bar{I}_{2}\right)^{1/2}I\right] \tag{27}$$

$$J\mathscr{C}_{\mathrm{dev}} = -\frac{2}{3}\left(\bar{h}\otimes I + I\otimes\bar{h}\right) + \frac{2}{3}\,\mathrm{tr}(\bar{h})\left(\tilde{I} + \frac{1}{3}I\otimes I\right) + \frac{2}{3}\beta\mathrm{tr}\left(\frac{\partial\bar{\bar{\Psi}}^{0}}{\partial\bar{E}}\right)\left(\tilde{I} - \frac{1}{3}I\otimes I\right)$$
$$+ J\beta\bar{\mathscr{C}}^{0} - \frac{J\beta}{3}\left[\left(\bar{\mathscr{C}}^{0}{:}I\right)\otimes I + I\otimes\left(\bar{\mathscr{C}}^{0}{:}I\right)\right] + \frac{J\beta}{9}\left(I{:}\bar{\mathscr{C}}^{0}{:}I\right)I\otimes I \tag{28}$$

where $\bar{h} = \bar{F}H\bar{F}^{\mathrm{T}}$, $\frac{\partial\bar{\bar{\Psi}}^{0}}{\partial\bar{E}} = \bar{F}\frac{\partial\bar{\Psi}^{0}}{\partial\bar{E}}\bar{F}^{\mathrm{T}}$ and $\bar{\mathscr{C}}^{0}_{ijkl} = \frac{1}{J}\bar{F}_{ip}\bar{F}_{jq}\bar{F}_{kr}\bar{F}_{ls}\left(\frac{\partial^{2}\bar{\Psi}^{0}}{\partial\bar{E}^{2}}\right)_{pqrs}$

The unsymmetric feature of $\mathscr{C}_f$ in Eq. (27) produces the unsymmetric stiffness matrix in the finite element analysis. For the sake of computational efficiency, symmetric approximation of $\mathscr{C}_f$, $(\mathscr{C}_f)_{\text{sym}} = \frac{1}{2}(\mathscr{C}_f + \mathscr{C}_f^T)$, is used. Substituting Eq. (26) for Eq. (18), the final form of tangent stiffness can be written as follows:

$$\mathscr{L}^J_{ijkl} = D_{\text{v}}\left[\left(\alpha J\frac{\partial^2 U^0}{\partial J^2} + P\right)\delta_{ij}\delta_{kl} - 2P\delta_{ik}\delta_{jl}\right] + D_{\text{d}}(\mathscr{C}_{\text{dev}})_{ijkl} + (\mathscr{C}_f)_{ijkl} + \delta_{ik}\sigma_{jl} + \sigma_{ik}\delta_{jl} \tag{29}$$

In this study, Mooney–Rivlin hyper elastic model is used for the deviatoric free energy function and second degree polynomials of J for the volumetric free energy function.

$$\bar{\Psi}^0 = \bar{C}_1(\bar{I}_1 - 3) + C_2(\bar{I}_2 - 3) \tag{30}$$

$$U^0 = \frac{K}{2}(J-1)^2 \tag{31}$$

Therefore, $\frac{\partial^2 U^0}{\partial J^2}$ and $\frac{\partial^2 \bar{\Psi}^0}{\partial \bar{E}^2}$ yield following.

$$\frac{\partial^2 U^0}{\partial J^2} = K \tag{32}$$

$$\frac{\partial^2 \bar{\Psi}^0}{\partial \bar{E}^2} = 4\bar{C}_2(I \otimes I - \tilde{I})$$

As stated above, the stress and tangent stiffness components are calculated in UMAT from Eq. (14), (29). The algorithm implemented in a computer code for the prediction of stress–strain behavior can be summarized as follows:

Initial propellant properties and configuration:
1. Specify mechanical properties of the solid propellant, matrix, filler, void and adhesion energy
2. Specify initial statistical distribution of filler particle size.

Deformation of solid propellant:
3. Calculate the cyclic loading damage function by Eq. (12)
4. Calculate the viscoelastic stress by Eq. (14)
5. Check, with Eq. (7), whether dewetting occurs at this stress for the largest particles
6. If dewetting do not occurs, calculate tangent modulus by Eq. (29) and go to ABAQUS main routine.
7. If dewetting occurs, reduce the dewetted filler volume fraction and increase the void volume fraction by the same amount.
8. Calculate the reduced relaxation modulus and damage functions by Eqs. (8), (6) and (9).
9. Reduce the current filler volume fraction by the dewetted filler amount.
10. Go to STEP 4 and calculate the reduced nonlinear viscoelastic stress by Eq. (14).

This process is summarized in the flow chart shown in Fig. 5.

4. Experiment

The material used in this study is an HTPB solid propellant with 76% particle volume fraction of AP

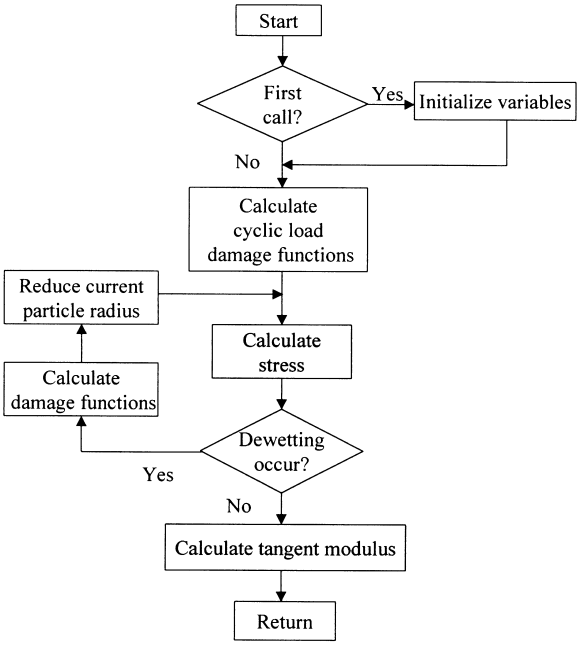

Fig. 5. Calculation algorithm for UMAT.

(ammonium perchlorate) and Al (aluminum) powder. The initial propellant properties and configuration required in the simulation were measured (Jung and Youn, 1999). Moduli were obtained from uniaxial, shear relaxation tests and Pockerchip constant rate tests at −90 to 60°C as shown in Fig. 6. Adhesion energy between binder and AP was obtained from 180° peel test. Moduli of the void were determined by

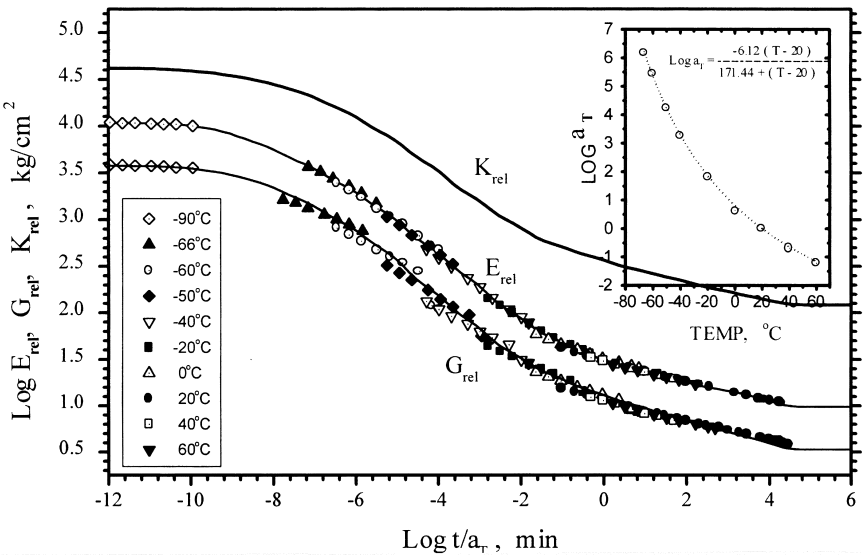

Fig. 6. Master relaxation modulus and shift factor.

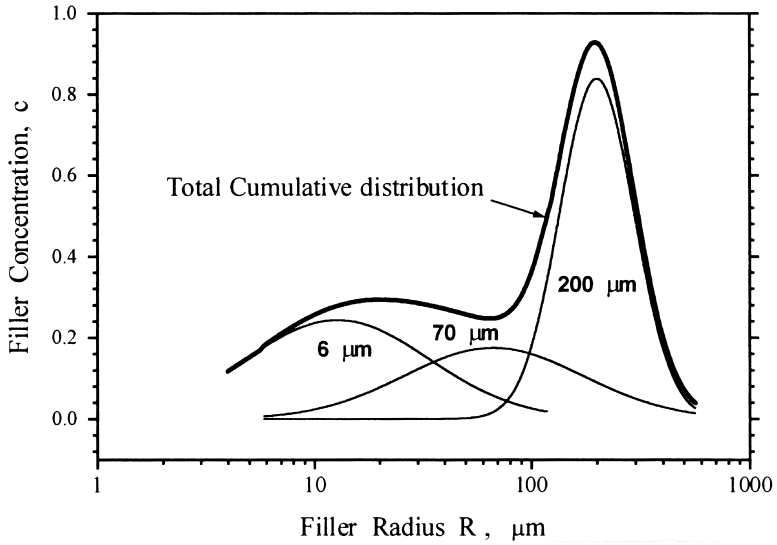

Fig. 7. Filler size distribution for the solid propellant used.

matching the uniaxial constant rate stress–strain curve at 20°C, 50%/min. Statistical distribution of filler particle size was measured by a Malvern Series Particle sizer and the result is shown in Fig. 7. The methods to obtain these parameters and the results are explained in detail in the previous paper by the same authors (Jung and Youn, 1999).

The biaxial strip tests are conducted to verify the validity of the three-dimensional constitutive model. The strip biaxial specimen is rectangular in shape and bonded to wooden-tab as illustrated in Fig. 8 (Schapery et al., 1975). The specimen contains a circular hole to produce severe stress gradients. A large block of the material is bonded to wooden-tab with the polyurethane adhesive and specimens are mill machined out of the block. The specimens are stored in a desicator (RH < 10%) to minimize the effects of humidity. Constant rate tests, complex load tests are conducted. Four specimens are tested at one test condition and stress responses are averaged. All tests are performed in an Instron 1122 and gas dilatometer in the humidity controlled room (RH < 30%). Prior to testing, the specimens are conditioned at each test temperature for more than 1 h.

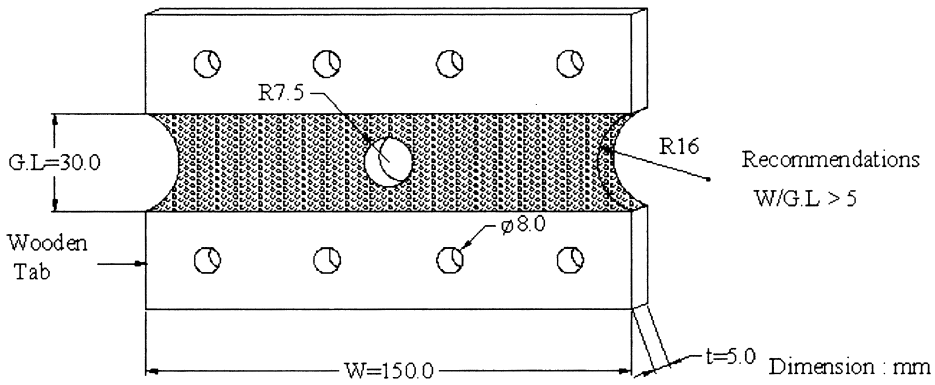

Fig. 8. Biaxial specimen geometries and dimensions.

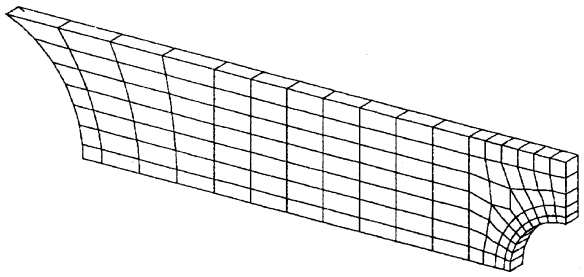

Fig. 9. Finite element mesh models of biaxial specimen.

5. Finite element analysis

Finite element mesh model of the specimen is shown in Fig. 9. One-eighth specimen is modelled using the symmetry conditions. Twenty noded, three-dimensional isoparametric elements are used to model the specimens. Finite element analyses are conducted for the loading conditions tested. The initial time increment equivalent to the 0.5% global strain is chosen for the analysis. Auto time increment and the convergence criteria in ABAQUS are applied.

6. Results and discussion

6.1. The constant rate test

The biaxial specimen is loaded at constant strain rates, 66.7 and 0.67%/min and temperatures, 60, 20, and −40°C. The comparisons between the predicted and measured responses are shown in Figs. 10–12. Global stress and volume dilatation against global strain is plotted. Global strain means the displacement divided by the specimen height and global stress the load divided by the minimum cross

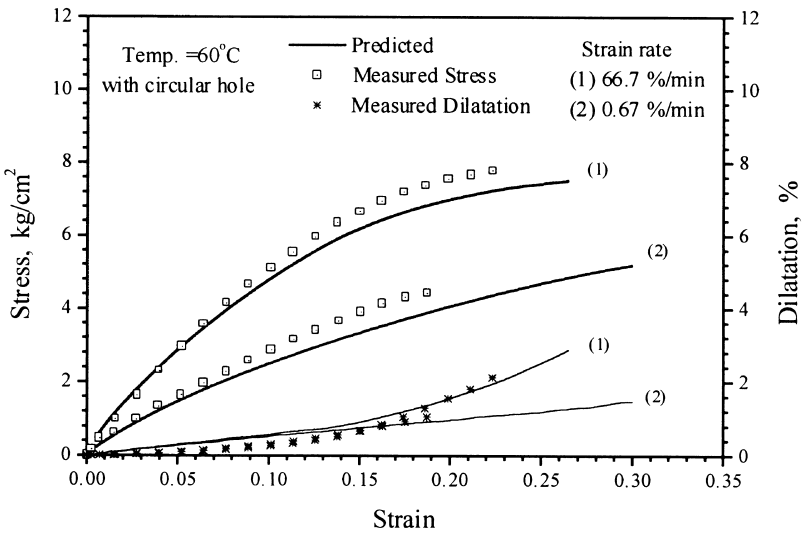

Fig. 10. Biaxial constant strain rate test at 60°C.

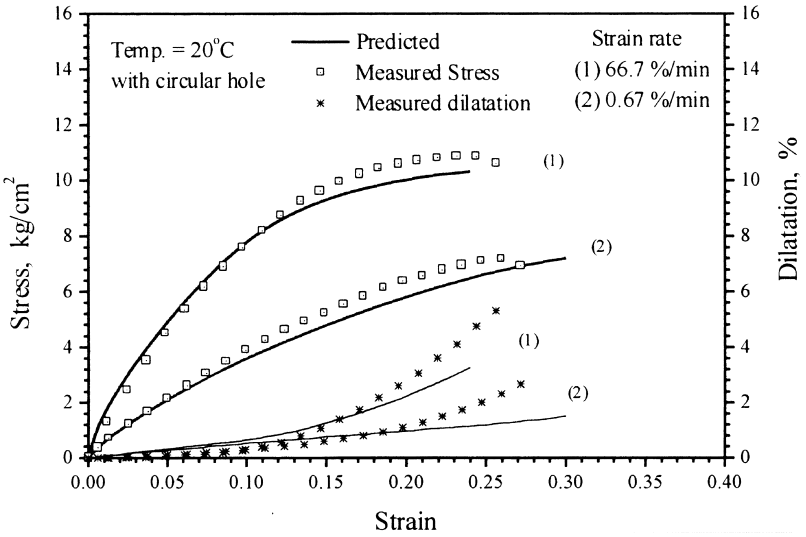

Fig. 11. Biaxial constant strain rate test at 20°C.

section area of the specimen. A specimen with a hole creates a strain concentration around the perimeter of the hole, the crack initiate at either side of the hole at the global strain lower than the uniaxial test. The maximum values of each measured strain represent the crack initiation points. The finite element analysis is conducted to the global strain of 30%. For some loading conditions, the solutions do not converge up to the 30% global strain. This nonconvergent point corresponds to the one that the maximum stress in the specimen reaches the tensile strength of the propellant. In this case, the norm of tangent stiffness approaches zero and the material instability occurs. In reality, the crack initiates at this nonconvergent stress value. In general, the predicted stress responses are in good agreement with the measured ones for the various strain rates and temperatures. The current model is verified for the

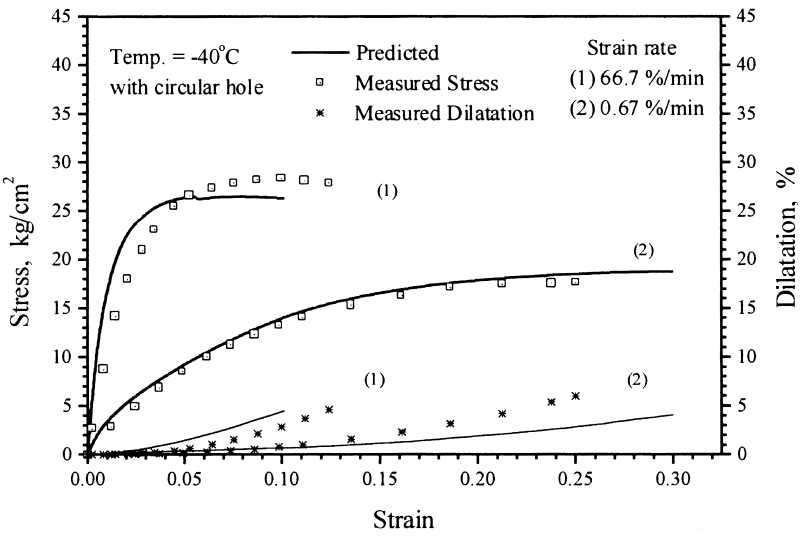

Fig. 12. Biaxial constant strain rate test at −40°C.

biaxial geometry in addition to the uniaxial one (Jung and Youn, 1999). This demonstrates the validity of the model which treats the softening of the propellant by the modulus decrease due to viscoelastic dewetting. The calculated dilatations are distributed somewhat lower than the measured values. However their trends are shown to be consistent.

6.2. Constant cyclic test

Cyclic load is applied to the biaxial specimen at 20°C. The test is done with five cycles at global strain levels of 0–17.6% and strain rate 66.7%/min. There is a good agreement between the predicted and measured stress as shown in Fig. 13. Thus the unloading and reloading functions obtained from one uniaxial cyclic test condition can be used for the biaxial case. The applicability of cyclic load damage function is verified.

6.3. Similitude test

The biaxial specimen is loaded at strain rate 1.67%/min to the global strain level 12.3% and then allowed to relax for 3 h. The relaxation is repeated at the global strain of 3.3% for 2 h and then the specimen is loaded to failure at 6.7%/min. While the relaxation response is somewhat over-predicted, the loading portions are well predicted as shown in Fig. 14. The results show the applicability of the model for the relaxation and loading conditions.

6.4. Straining and cooling test

The tests are intended to verify the model for the loads that the solid propellant grains usually experience. The biaxial specimen is cyclic loaded with the temperature lowering at a constant rate. The first test is done with the increasing strain amplitude 0–22.3% at 1.67%/min, while the temperature is changed at −1°C/min from 38°C as shown in Fig. 15. Another cyclic test with subsequent loading and unloading at different strain levels is also conducted with the same strain rate of 1.67%/min while the

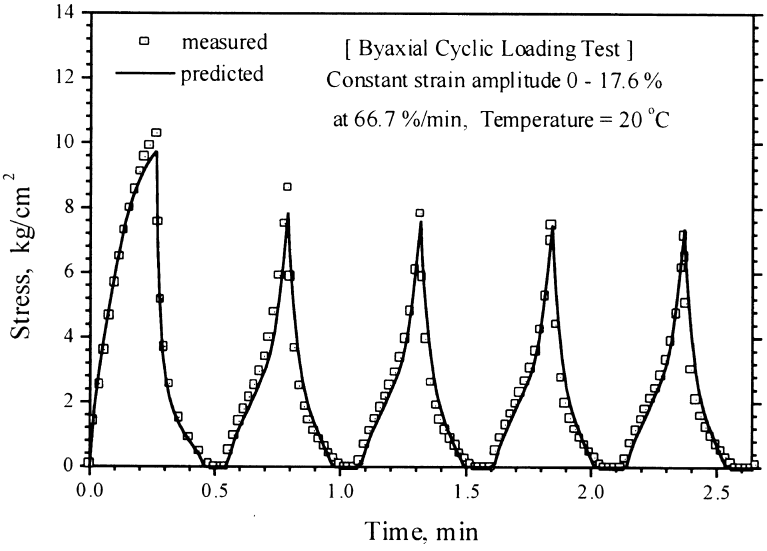

Fig. 13. Biaxial cyclic test with constant strain amplitude at 20°C.

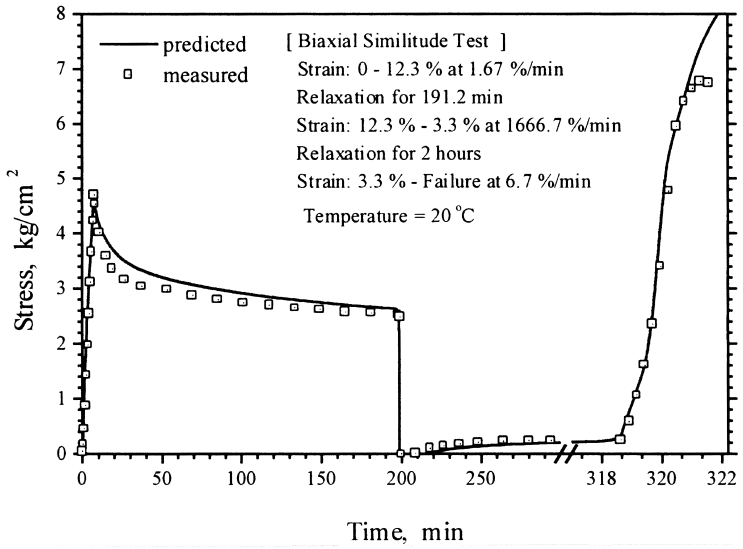

Fig. 14. Biaxial similitude test at 20°C.

temperature is changed at −1°C/min from 27°C as shown in Fig. 16. As shown in Figs. 15 and 16, the model somewhat under-predicts the magnitude of the stress. The predicted stresses are close enough to the measured ones. Also, as shown in Fig. 16, the stresses are accurately predicted for the reloading or unloading from reloading conditions. The results clearly demonstrate that the model can be used to predict the complex behavior of the propellant.

As mentioned above, the constitutive model predicts reasonably well the solid propellant behaviors under multi-axial and complex loading conditions that consist of constant loading, cyclic loading, relaxation and straining and cooling. The model uses the damage functions developed from a few uniaxial tests (Jung and Youn, 1999). The accuracies of the biaxial stresses and dilatation are somewhat

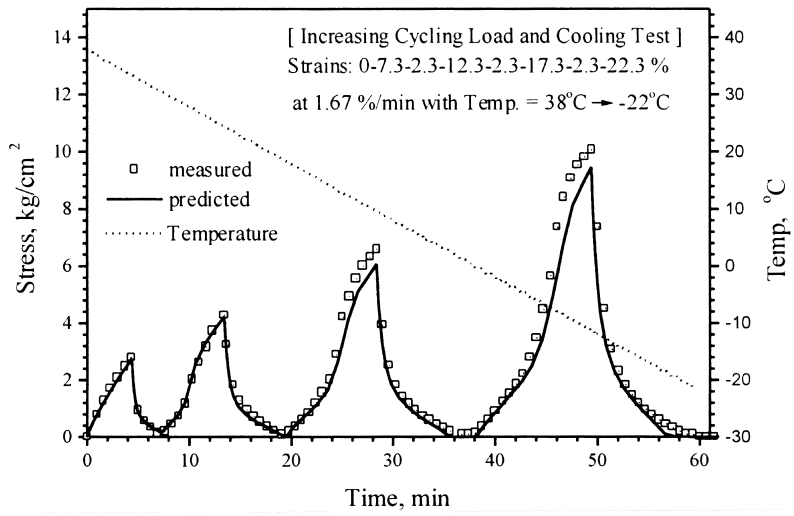

Fig. 15. Biaxial cycling with increasing strain amplitude and cooling test.

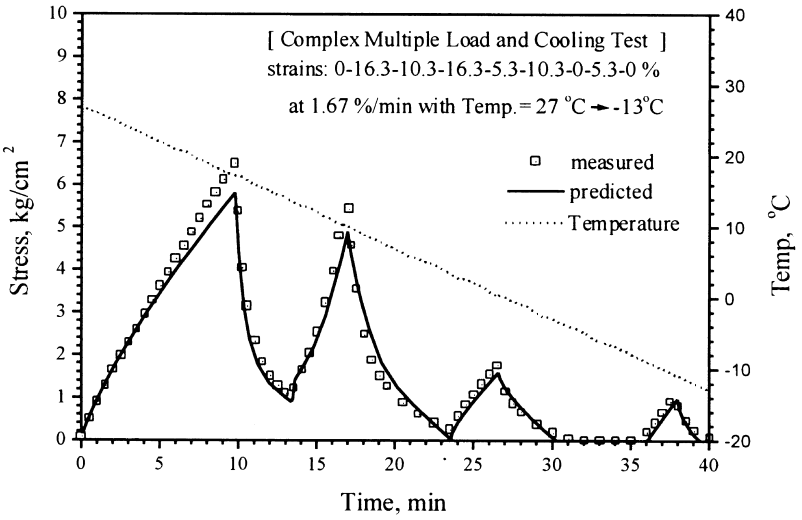

Fig. 16. Biaxial complex multiple load and cooling test.

lower than the uniaxial cases (Jung and Youn, 1999). However, the predicted values are very close to the measured ones.

6.5. Comparison with other models

The comparisons with other models are impossible because the filler particle distributions and adhesion data needed in current model are not available in the references of other models. Also, the implementations of other models require some large amount of experiments and programming to characterize the damage functions. So, the comparisons are made for the results predicted by the constitutive models used in ABAQUS, TEXPAC code (Becker and Miller, 1989) and current model. The

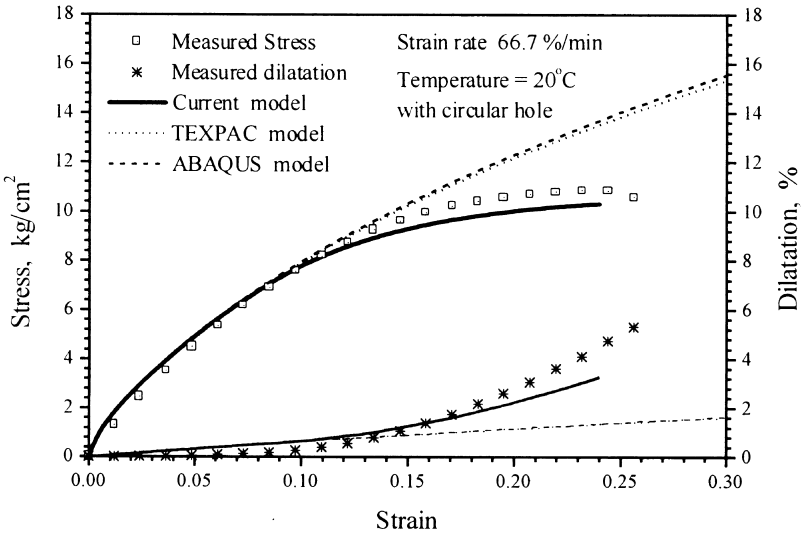

Fig. 17. Comparisons of Current model, TEXPAC model and ABAQUS model at constant strain rate test at 20°C.

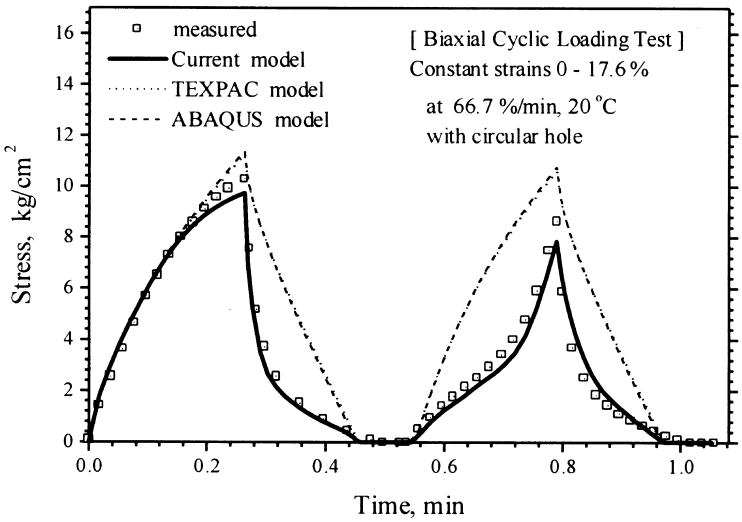

Fig. 18. Comparisons of Current model, TEXPAC model and ABAQUS model at cyclic test at 20°C.

constitutive model in ABAQUS (finite strain viscoelasticity model) suitably generalizes the linear viscoelastic hereditary integral to finite strain formulation. The model in TEXPAC adopted the Simo's viscoelastic constitutive model. These two models can be used for viscoelastic material, which is homogeneous and capable of large deformation without damage. But it is inappropriate to apply these models to composite viscoelastic materials like solid propellant where damages are unavoidable when in

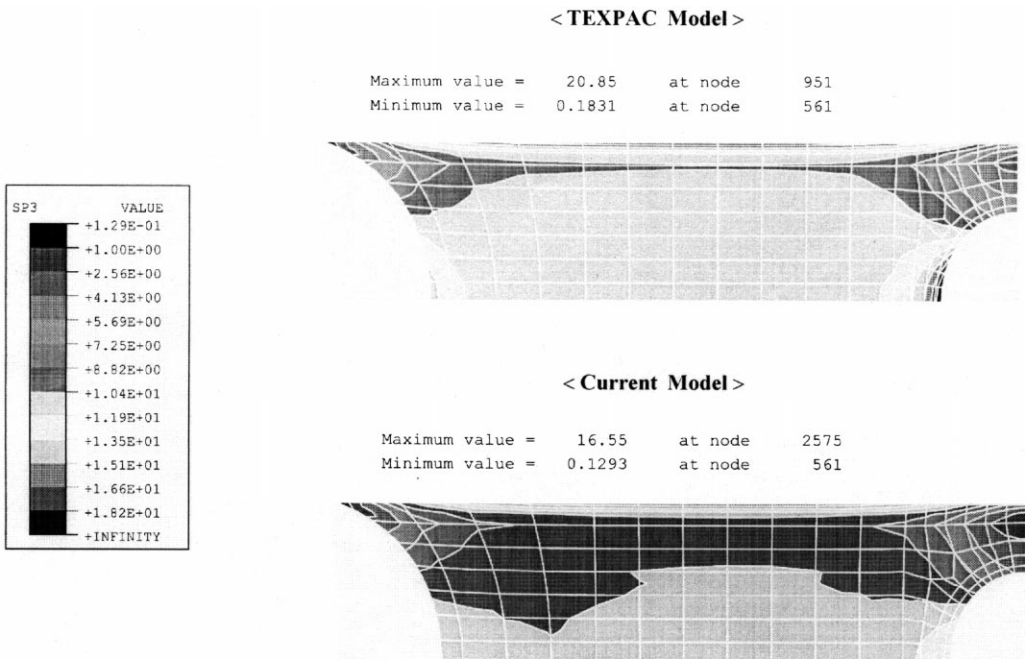

Fig. 19. Comparison of the maximum principal stress distributions in the biaxial specimen between TEXPAC model and Current model at global strain 15%.

use. For the loading conditions of constant rate test and constant cyclic test (for the case of Figs. 11 and 13), the predicted and measured responses are shown in Figs. 17 and 18,. The predicted results by ABAQUS and TEXPAC are almost the same. As the strain increases, the predicted stress response by ABAQUS and TEXPAC over-estimates the measured values and the over-estimation become more conspicuous for the cyclic loading. This is due to the fact that material nonlinearities are not considered in the constitutive models used in ABAQUS and TEXPAC. The comparisons of the stress distributions at global strain 15% are shown in Fig. 19. This distribution is from the biaxial constant strain rate test at 20°C, strain rate 66.7%/min as shown in Fig. 11. In Fig. 11, dilatation is about 1.2% and the dilatation against strain slope is larger than the one at small strain range. This indicates that dewetting is involved. This can also be predicted from the dewetting criterion. Of course, the dewetting occurs in the high stress concentration area around the hole and the stress distribution is much different at this region. Therefore, the TEXPAC model produces higher stresses than current model. These results show the importance of considering the material nonlinearities into the constitutive model.

7. Conclusions

A three-dimensional nonlinear viscoelastic constitutive model of composite solid propellant is developed and tested for biaxial loading conditions. In the model, the cyclic loading damage function of Özüpek and Becker that is based on the octahedral shear strain measure is modified to improve the stress prediction accuracy. The constitutive equation is implemented into a finite element analysis code for the analysis of biaxial specimens. A commercial finite element package 'ABAQUS' is adopted for analysis and the developed constitutive equation is implemented through a user subroutine, UMAT. The constitutive model has been tested for biaxial complex loading conditions and the predictions have been compared with the experiments. The results show that the model predicts the broad range of the propellant behaviors with reasonable accuracies. Also, the importance of the material nonlinearities is demonstrated through the comparisons with the constitutive models in ABAQUS and TEXPAC for certain loading conditions. Therefore, the developed constitutive model can be effectively used in the three dimensional finite element analysis for solid propellant grains.

References

Becker, E.B., Miller, T., 1989. User's Manual for the TEXPAC Computer Code. MSI, Austin, TX.

Farber, J.N., Farris, R.J., 1987. Model for prediction of the elastic response of reinforced materials over wide ranges of concentration. J. Appl. Polym. Sci 34, 2093–2104.

Farris, R.J., Schapery, R.A. 1973. Development of a Solid Rocket Propellant Nonlinear Viscoelastic Constitutive Theory. AFRPL-TR-73-50.

Hibbit, Karlsson and Sorenson, Inc. 1996. ABAQUS User's Manual, version 5.6.

Hibbit, Karlsson and Sorenson Inc. 1996. ABAQUS Theory Manual, version 5.6.

Jung, G.D., Youn, S.K., 1999. A nonlinear viscoelastic constitutive model of solid propellant. Int. J. Solids Structures 36, 3755–3777.

Özüpek, S., Becker, E.B., 1996. Constitutive equations for solid propellants. Int. J. Engng. Mat. Tech 119, 125–132.

Park, S.W., Schapery, R.A., 1997. A viscoelastic constitutive model for particulate composites with growing damage. Int. J. Solids Structures 34, 931–947.

Ravichandran, G., Liu, C.T., 1995. Modelling constitutive behavior of particulate composites undergoing damage. Int. J. Solids Structures 32, 979–990.

Taylor, R.L., Pister, K.S., Goudreau, G.L., 1970. Thermomechanical analysis of viscoelastic solids. Int. J. Numer. Methods Eng 2, 45–59.

Schapery, R.A., et al., 1975. Solid Propellant Mechanical Behavior Manual. CPIA Pub. 21.

Simo, J.C., 1987. On a fully three-dimensional finite strain viscoelastic damage model: formulation and computational aspects. Computer Methods in Applied Mechanics and Engineering 60, 153–173.

Swanson, S.R., Christensen, L.W., 1983. A constitutive formulation for high elongation propellant. J. Spacecraft 20, 559–566.